

# Titanium dioxide nanoparticles dispersed in heteroatom-doped carbon nanofibers for ultrafast lithium storage

Ki-Wook Sung and Hyo-Jin Ahn\*

Department of Materials Science and Engineering, Seoul National University of Science and Technology, Seoul 01811, Korea

Titanium dioxide (TiO<sub>2</sub>) is a promising anode material for lithium-ion batteries (LIBs) owing to its low price, excellent cycling stability, low operating voltage, and environmentally friendly nature. However, owing to their poor electrical and ionic diffusion, TiO<sub>2</sub> anodes show low specific capacity and poor high-rate performance. In this study, in an attempt to improve the electrical and ionic diffusion properties, we dispersed TiO<sub>2</sub> nanoparticles into N- and P-doped carbon nanofibers (N/P-doped CNF/TiO<sub>2</sub>) using the hydrothermal, electrospinning, and carbonization processes. The N/P-doped CNF/TiO<sub>2</sub> electrode showed high specific capacity (311.5 mAh g<sup>-1</sup> at 100 mA g<sup>-1</sup> after 100 cycles), outstanding high-rate performance (286 mAh g<sup>-1</sup> at 2000 mA g<sup>-1</sup>), and excellent ultrafast cycling stability (285 mAh g<sup>-1</sup> at 2000 mA g<sup>-1</sup> after 500 cycles). The results showed that dispersing TiO<sub>2</sub> nanoparticles into N- and P-doped CNFs is an efficient approach to improve their electrical conductivity, shorten their lithium ion diffusion pathways, and stabilize the electrochemical conditions for ionic diffusion during ultrafast cycling.

**Keywords:** Lithium-ion batteries, TiO<sub>2</sub> nanoparticles, Carbon nanofibers, Heteroatom doping, Synergistic effect, Ultrafast cycling performance.

## Introduction

Over the past few years, the rapid depletion of fossil fuels and ecological concerns such as global warming and environmental pollution have tremendously increased the demand for environmentally friendly energy storage devices. Various energy storage devices such as supercapacitors, fuel cells, and lithium-ion batteries (LIBs) have gained immense attention as the main power source for electric vehicles (EVs). Among these energy storage devices, LIBs are widely used as the main power source for EVs because of their high energy density, long lifespan, low memory effect, and eco-friendliness [1-5]. However, LIBs suffer from long charging times. For instance, Tesla Model 3 EV requires a long charging time of 20-30 h at home or 5-6 h at a charging point [5, 6]. To overcome this limitation of EVs, LIBs with ultrafast charging/discharging, high capacity, and cycling stability have been developed [5, 7, 8].

As the storage rate of an anode is the limiting factor for its ultrafast charging, the performance of LIB anodes depends on their properties. In order to improve the cycling capacity and cycling stability of LIB anodes (metal, metal oxide, and non-metal), they are composited with carbon materials (graphite, graphene,

and carbon nanofibers) [9-11]. Titanium dioxide (TiO<sub>2</sub>) is a widely used anode material owing to its low cost, low volume expansion, and high cycling stability during the charging/discharging processes [12-15].

However, the low electrical conductivity and low lithium ion diffusivity of TiO<sub>2</sub> deteriorate the specific capacity and rate performance of TiO<sub>2</sub> LIB anodes [12, 16-18]. These limitations of TiO<sub>2</sub> LIB anodes can be overcome by forming composites with carbon nanofibers (CNFs), which exhibit high electrical conductivity (~100 S cm<sup>-1</sup>), high specific surface area (~621 m<sup>2</sup> g<sup>-1</sup>), and a one-dimensional network structure [5, 19-21].

Various studies have been carried out to improve the electrochemical behavior of carbon-based materials through surface modification by heteroatom doping [22-26]. Heteroatom doping improves the electrical conductivity and high structural stability of the carbon structure and provides a large number of active sites through the formation of defect sites by the carbon-heteroatom bonds [27]. The doped heteroatoms function as electron-rich or electron-deficient dopants, thus affecting the charge density around the carbon atoms and generating a large number of surface functional groups. These functional groups facilitate the absorption of electrolyte ions on the electrode surface, thus improving the cycling stability of the electrode [27, 28].

It is well-known that anionic dopants such as N and P improve the electrical conductivity, faradaic process activity, and structural stability of carbon-based materials by modifying the orbital structure of their bonds with

\*Corresponding author:  
Tel : +82-2-970-6622  
Fax: +82-2-973-6657  
E-mail: [hjahn@seoultech.ac.kr](mailto:hjahn@seoultech.ac.kr)

carbon [22, 27]. However, it is challenging to develop metal oxide-carbon nanocomposite structures (obtained through heteroatom doping) with ultrafast charging/discharging during cycling.

Thus, in this study, we dispersed TiO<sub>2</sub> nanoparticles (NPs) in N- and P-doped CNFs to develop LIB anodes (N/P-doped CNF/TiO<sub>2</sub>) with ultrafast charging/discharging. The TiO<sub>2</sub> NPs were fabricated using the hydrothermal method, and the N-/P-doped CNF/TiO<sub>2</sub> anodes were fabricated via electrospinning and calcination.

## Experiments

N/P-doped CNF/TiO<sub>2</sub> was fabricated via hydrothermal synthesis, electrospinning, and carbonization. First, in order to synthesize the TiO<sub>2</sub> NPs, titanium (IV) isopropoxide (C<sub>12</sub>H<sub>28</sub>O<sub>4</sub>Ti, 97%, Sigma-Aldrich) was dispersed in a solution of deionized (DI) water and ethylenediamine (C<sub>2</sub>H<sub>8</sub>N<sub>2</sub>, 99.5%, Sigma-Aldrich) under stirring for 2 h. This solution was transferred to an 80 mL Teflon-lined stainless-steel autoclave and stirred for 3 h. A hydrothermal reaction was carried out at 170 °C for 4 h. The samples were then washed five times with DI water and dried in an oven at 80 °C. In order to synthesize N/P-doped CNF/TiO<sub>2</sub>, ~15 wt% of the TiO<sub>2</sub> NPs and 10 wt% of polyacrylonitrile (PAN, M<sub>w</sub> = 150,000, Sigma-Aldrich, also known as vinyl cyanide) were dispersed in an N,N-dimethylformamide (DMF, 99.8%, Sigma-Aldrich) solution. For the electrospinning process, the needle was kept at 23 gauge, and the distance between the needle and the collector was 15 cm. The feeding rate and voltage were set at 0.03 mL h<sup>-1</sup> and 13 kV, respectively. A relative humidity of less than 15% was maintained in the electrospinning chamber.

For preparing the P-doped CNFs, stabilized NFs, which were heated at 200 °C for 2 h in air, were mixed with red P (M<sub>w</sub> = 30.97, Aladdin) in the ratio of 1: 3 and the resulting mixture was calcined at 800 °C for 2 h. The resulting P-doped CNFs were then used to prepare N/P-doped CNF/ TiO<sub>2</sub>. For comparison, N-doped CNF/TiO<sub>2</sub>, bare CNFs, and bare TiO<sub>2</sub> NPs were also prepared.

The morphologies and structures of all the samples were observed using field-emission scanning electron microscopy (FESEM, Hitachi S-4800) and transmission electron microscopy (MULTI/TEM; Tecnai G<sup>2</sup>, KBSI Gwangju Center). The crystal structures of the samples were examined using X-ray diffraction (XRD, Rigaku D/Max 2500V) over the 2θ range of 10-90° with a step size of 0.02°. As the CNF matrix decomposes over 450°C in an air atmosphere, thermogravimetric (TG, TGA-50) measurements were carried out over the temperature range of 200-900 °C at a heating rate of 10 °C min<sup>-1</sup> under an air atmosphere to calculate the carbon content within the samples. Thus, the carbon content of TiO<sub>2</sub> NPs, N-doped CNF/TiO<sub>2</sub>, and N/P-

doped CNF/TiO<sub>2</sub> were calculated as 0%, 31%, and 31%. The chemical bonding states of the samples were determined by X-ray photoelectron spectroscopy (XPS, ESCALAB 250) using Al K<sub>a</sub> X-ray sources. The porous structures of the samples were examined by obtaining their N<sub>2</sub> adsorption/desorption isotherms using the Brunauer-Emmett-Teller (BET) and Barrett-Hoyner-Halenda (BJH) methods.

The electrochemical performances of the samples were evaluated using coin-type cells (CR2032, Hohsen Corporation) with the prepared samples as the anode, a lithium metal foil (Honjo Chemical, 99.8%) as the cathode, a 1.0 M LiPF<sub>6</sub> solution in a mixture of ethylene carbonate-dimethyl carbonate (1:1) as the electrolyte, and a porous polypropylene membrane (Celgard 2400) used as the separator. To fabricate the anodes, a slurry was prepared using 70 wt% of the prepared samples, with 20 wt% of polyvinylidene fluoride as the binder, and 10 wt% Ketjenblack (Alfa Aesar) as the conducting material, in N-methyl-2-pyrrolidinone (Sigma-Aldrich). The homogenized slurry was coated on to a Cu foil (Nippon Foil, 18 mm) and then oven-dried at 100 °C for 12 h. All the coin-type cells were assembled in a high-purity argon-filled glove box (< 5 ppm H<sub>2</sub>O and O<sub>2</sub>).

Charging/discharging tests were carried out using a battery cycler system (WonATech Corp., WMPG 3000) over the potential range of 0.05-3.00 V (vs. Li/Li<sup>+</sup>) at 25 °C in an incubator. Cyclic voltammetry (CV) measurements were carried out on a potentiostat/galvanostat (EcochemieAutolab PGST302N) at the scan rate of 0.1 mV s<sup>-1</sup> over the potential range of 0.05-3.00 V (vs. Li/Li<sup>+</sup>).

The cycling stability of the samples was evaluated up to 100 cycles at a current density of 100 mA g<sup>-1</sup>. The high-rate cycling performance of the samples was observed for 10 cycles at the current densities of 100, 300, 500, 700, 1,000, and 2,000 mA g<sup>-1</sup>. The ultrafast cycling density of the samples was examined for 500 cycles at a current density of 2,000 mA g<sup>-1</sup>. Electrochemical impedance spectroscopy (EIS) measurements were carried out using fresh cells over the frequency range of 10<sup>5</sup>-10<sup>-2</sup> Hz by applying an AC signal of 5 mV.

## Results and Discussion

As shown in Fig. 1, the N/P-doped CNF/TiO<sub>2</sub> sample was synthesized via electrospinning and carbonization. For the electrospinning process, the TiO<sub>2</sub> NPs prepared using the hydrothermal process and PAN were stirred in DMF. The as-spun NFs with TiO<sub>2</sub> NPs embedded in the PAN NFs were collected as shown in Fig. 1(a). The as-spun NFs were stabilized, mixed with red P, and carbonized at 800 °C for 2 h in a nitrogen atmosphere. The red P and N atoms (donated by the PAN NFs) yielded N/P-doped CNFs (Fig. 1(b)).

Fig. 2 shows the FESEM images of the TiO<sub>2</sub> NP,

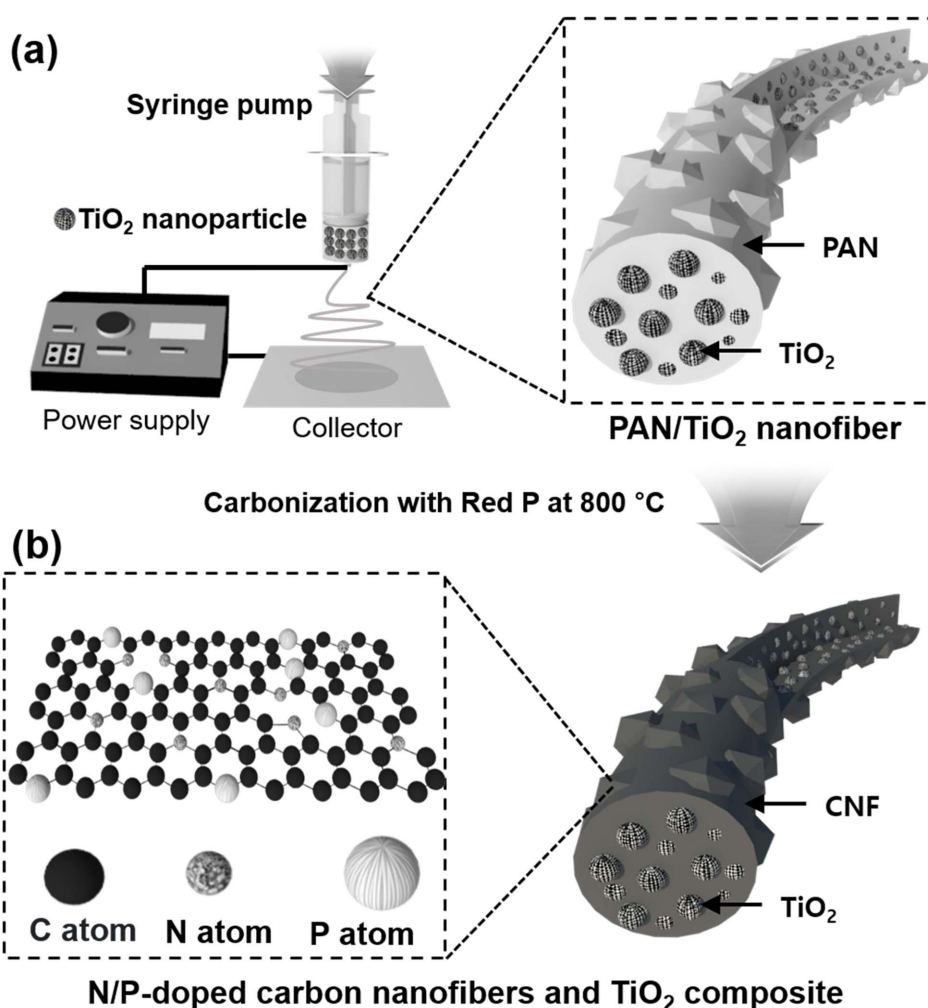


**Fig. 1.** Schematic illustration of synthetic process for N/P-doped C/ $\text{TiO}_2$ . (a) The stabilized PAN/ $\text{TiO}_2$  nanofibers after electrospinning process using  $\text{TiO}_2$  nanoparticles and PAN in DMF solution. (b) N/P-doped CNF/ $\text{TiO}_2$  after carbonization with red P.

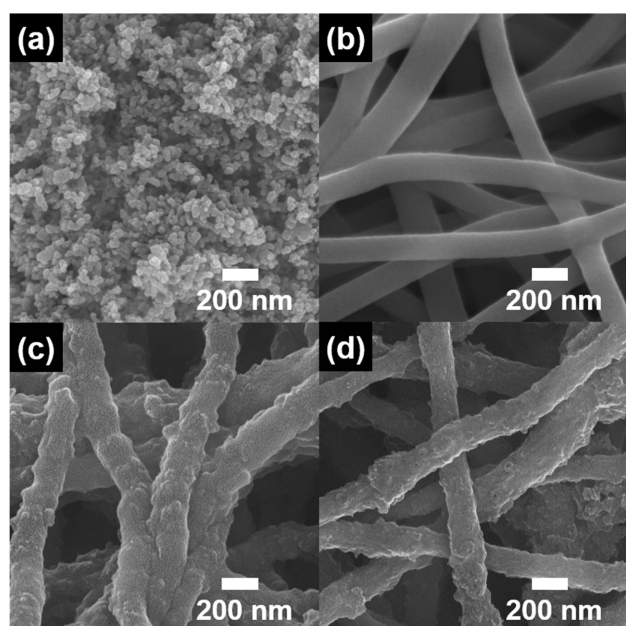


**Fig. 2.** FESEM images of  $\text{TiO}_2$ , bare CNFs, N-doped CNF/ $\text{TiO}_2$ , N/P-doped CNF/ $\text{TiO}_2$ .

bare CNF, N-doped CNF/ $\text{TiO}_2$ , and N/P-doped CNF/ $\text{TiO}_2$  samples. The  $\text{TiO}_2$  NPs were found to be  $\sim 37\text{-}46$  nm in size, while bare CNFs showed a diameter of  $\sim 147\text{-}189$  nm (Figs. 2(a) and 2(b)). N-doped CNF/ $\text{TiO}_2$  and N/P-doped CNF/ $\text{TiO}_2$  (Figs. 2(c) and 2(d)) with the diameters of  $\sim 179\text{-}220$  and  $\sim 155\text{-}206$  nm, respectively, showed bumpy fiber structures because of the distribution of  $\text{TiO}_2$  NPs in their CNF matrices. Because of the presence of one-dimensional NFs, the composites showed an interconnected network structure, which improved their electron transfer and lithium-ion diffusion rates, thus improving the LIB performance [29-32]. In addition, when P was doped onto the surface of the CNFs, the carbon atoms in the C-C bonds were replaced by P atoms. This is because the atomic radius of P (1.1 Å) is larger than that of C (0.77 Å). Moreover, P doping increased the surface roughness of the CNFs through lattice expansion.

To further examine the structure of the well-dispersed  $\text{TiO}_2$  NPs in the N/P-doped CNFs, TEM analysis was carried out. Fig. 3 shows the low-resolution (Fig. 3(a)) and high-resolution (Fig. 3(b)) TEM images of the N/

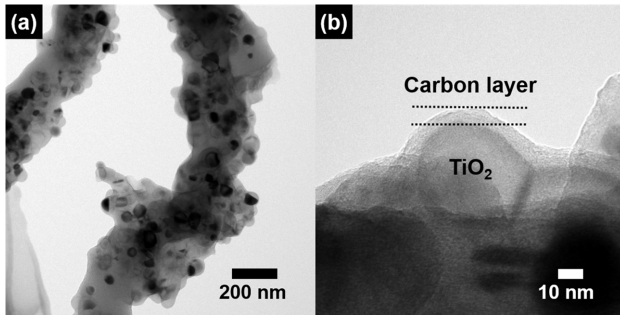


**Fig. 3.** Low-resolution (a) and high-resolution (b) images of N/P-doped C/TiO<sub>2</sub>.

P-doped CNF/TiO<sub>2</sub> composite. The TiO<sub>2</sub> NPs were ~37-46 nm in diameter and were well-dispersed in the CNF matrix (Fig. 3(a)). Fig. 3(b) shows that the TiO<sub>2</sub> NPs were coated with a carbon layer. Thus, the well-dispersed TiO<sub>2</sub> NPs increased the electrical conductivity of the CNFs, which in turn improved the lithium ion intercalation/deintercalation kinetics of the composite by reducing the lithium ion diffusion length.

The crystal structures of the TiO<sub>2</sub> NP, bare CNF, N-doped CNF/TiO<sub>2</sub>, and N/P-doped CNF/TiO<sub>2</sub> samples were analyzed by XRD (Fig. 4(a)). The TiO<sub>2</sub> NPs showed peaks at  $2\theta = 27.6^\circ$ ,  $36.2^\circ$ , and  $54.6^\circ$  corresponding to the (110), (101), and (211) planes of the main rutile phase, respectively. The anatase peaks were observed at  $2\theta = 25.3^\circ$ ,  $37.8^\circ$ , and  $48.1^\circ$  corresponding to the (101), (004), and (200) planes, respectively [33]. The bare CNFs exhibited a broad diffraction peak at  $2\theta = 25^\circ$ , corresponding to the (002) plane of graphite [34]. The N-doped CNF/TiO<sub>2</sub> composite showed a broad diffraction peak at  $2\theta = 25^\circ$  corresponding to the (002) plane of graphite along with TiO<sub>2</sub> diffraction peaks. This indicates that this composite consisted of both the TiO<sub>2</sub> and CNF phases. The N/P-doped CNF/TiO<sub>2</sub> composite showed the same diffraction peaks as those shown by the N-doped CNF/TiO<sub>2</sub> composite, indicating

that P doping did not affect the crystal structure of the N-doped CNF/TiO<sub>2</sub> composite.

TGA were carried out to determine the concentrations of the TiO<sub>2</sub> NP, N-doped CNF/TiO<sub>2</sub>, and N/P-doped CNF/TiO<sub>2</sub> samples. No weight loss was observed for the TiO<sub>2</sub> NPs with an increase in temperature (Fig. 4(b)), indicating that these NPs did not contain any impurities. The N-doped CNF/TiO<sub>2</sub> and N/P-doped CNF/TiO<sub>2</sub> composites showed a weight loss of 69% because of the presence of carbon in them. In addition, as the P doping resulted in the breakage of the CNF bonding structure, the N/P-doped CNF/TiO<sub>2</sub> composite showed initial weight loss at a temperature lower than that for the N-doped CNF/TiO<sub>2</sub> composite.

XPS measurements were carried out to investigate the chemical bonding states of the samples. The Ti 2p XPS profiles (Figs. 4(a-c)) of the samples could be deconvoluted into two peaks at ~464.6 and ~458.9 eV corresponding to the Ti 2p<sub>1/2</sub> and Ti 2p<sub>3/2</sub> orbitals, respectively [35]. The TiO<sub>2</sub> NPs did not exhibit N 1s and P 2p peaks (Figs. 4(d) and 4(g)). The N 1s spectra of the N-doped CNF/TiO<sub>2</sub> and N/P-doped CNF/TiO<sub>2</sub> samples could be deconvoluted into four peaks at ~401.0, ~399.5, ~398.3, and ~403.3 eV corresponding to the pyrrolic-N, graphitic-N, pyridinic-N, and pyridine-N-oxide bonding states, respectively (Figs. 4(e) and 4(f)) [36]. This indicates that the N-doped CNF/TiO<sub>2</sub> and N/P-doped CNF/TiO<sub>2</sub> composites were well-doped with the nitrogen atoms from the PAN chains [37]. In general, pyrrolic-N and pyridinic-N increase the number of active sites in a composite owing to the fracturing of their carbon bonding states. Pyrrolic-N and pyridinic-N were formed at the edge sites of the carbon lattice and offered one or two p-electrons through the aromatic  $\pi$  system, increasing the electrical conductivity of TiO<sub>2</sub> [36]. In addition, the N-doped CNF/TiO<sub>2</sub> composite did not exhibit P 2p XPS peaks (Fig. 4(h)). On the other hand, the N/P-doped CNF/TiO<sub>2</sub> sample exhibited a P 2p XPS peak at ~132.5 eV corresponding to P-C

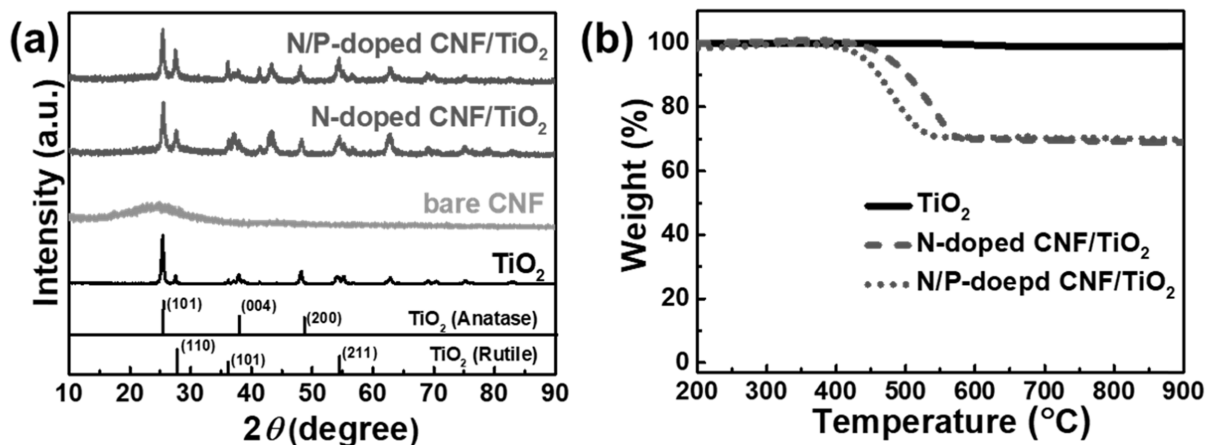


**Fig. 4.** (a) The XRD patterns of TiO<sub>2</sub>, bare CNFs, N-doped CNF/TiO<sub>2</sub>, and N/P-doped C/TiO<sub>2</sub>. (b) TGA curves of TiO<sub>2</sub>, N-doped CNF/TiO<sub>2</sub>, N/P-doped CNF/TiO<sub>2</sub> from 200 to 900°C at heating rate of 10°C min<sup>-1</sup> under air.

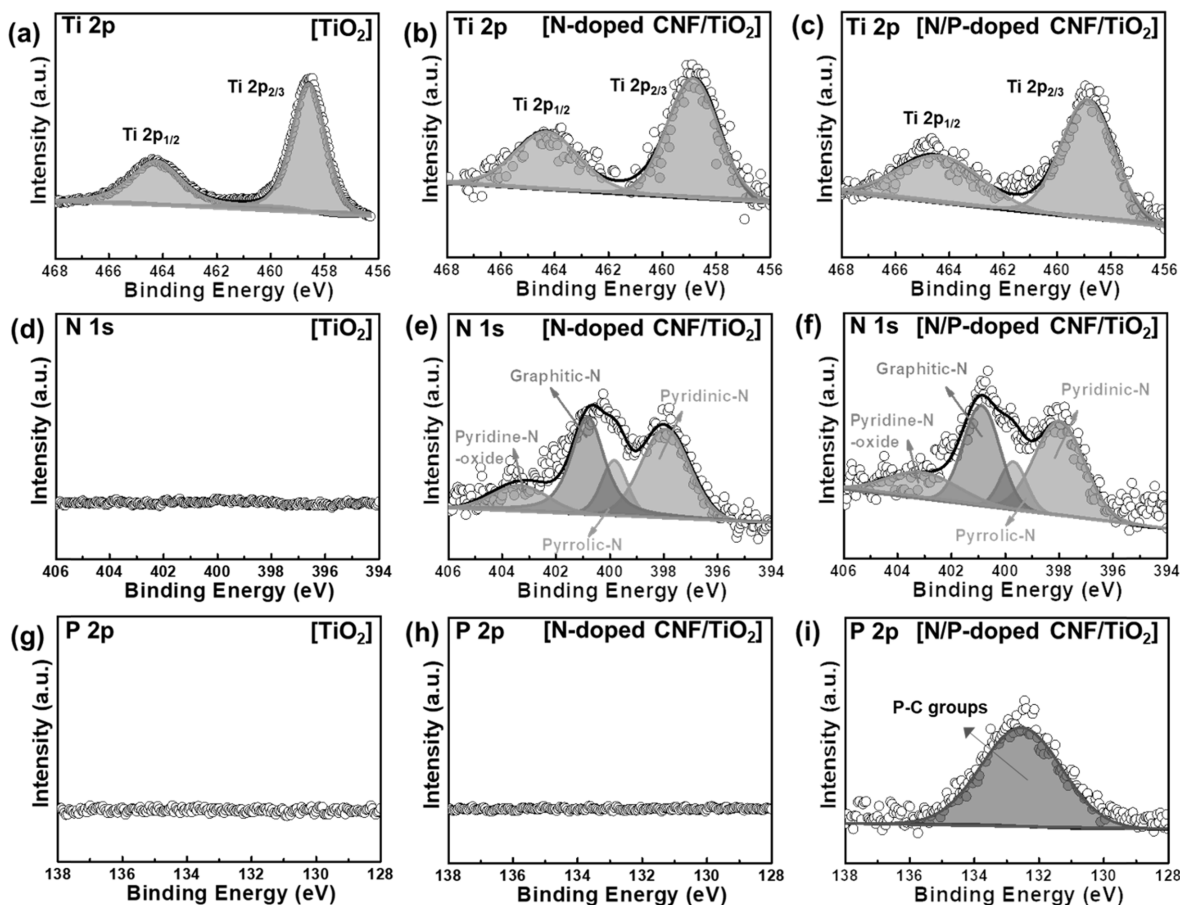


Fig. 5. XPS spectra of Ti 2p, N 1s, P 2p of  $\text{TiO}_2$  (a, d, and g), N-doped C/ $\text{TiO}_2$  (b, e, and h), and N/P-doped C/ $\text{TiO}_2$  (c, f, and i).

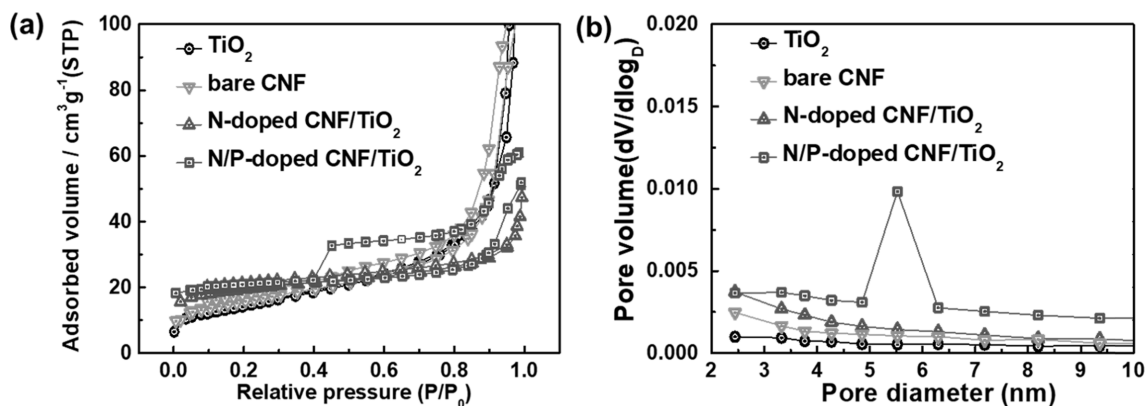


Fig. 6. (a) The  $\text{N}_2$  adsorption/desorption isotherms. (b) The BJH pore size distributions of  $\text{TiO}_2$ , bare CNF, N-doped C/ $\text{TiO}_2$ , and N-P doped C/ $\text{TiO}_2$ .

bonding groups (Fig. 4(i)). As the anionic radius of P is larger than that of C, the doped P atoms increased the specific surface area of the CNFs, which improved the high-rate capacity, electrical conductivity, and specific area of the N/P-doped CNFs/ $\text{TiO}_2$  composite.

The porous structures of the  $\text{TiO}_2$  NP, bare CNF, N-doped CNF/ $\text{TiO}_2$ , and N/P-doped CNF/ $\text{TiO}_2$  samples were examined by obtaining their  $\text{N}_2$  adsorption/desorption isotherms using the BET method (Fig. 6). The  $\text{TiO}_2$  NP, bare CNF, and N-doped CNF/ $\text{TiO}_2$  samples

exhibited type-I isotherms, indicating the presence of micropores (pore width,  $<2$  nm, as classified by the International Union of Pure and Applied Chemistry) [37, 38]. The N/P-doped CNF/ $\text{TiO}_2$  composite showed a type-IV isotherm, indicating the presence of mesopores (pore width, 2-50 nm) at high pressures ( $P/P_0 > 0.4$ ) [37, 38]. In other words, the N/P-doped CNF/ $\text{TiO}_2$  composite showed different isotherm intervals, indicating that it showed a mesoporous structure. The specific surface areas, total pore volumes, average pore diameters, and

pore volume fractions of all the samples are listed in Table 1. It can be observed from the table that the N/P-doped CNF/TiO<sub>2</sub> composite exhibited higher mesopore volume fraction than the TiO<sub>2</sub> NPs, bare CNF, and N-doped CNF/TiO<sub>2</sub> samples. To further investigate the pore sizes and volumes of the samples, BJH measurements were carried out. The results showed that the N/P-doped CNF/TiO<sub>2</sub> composite had high mesopore volume and a pore size of 5-7 nm. Owing to the difference in the atomic radii of C and P atoms, the doped P atoms increased the specific surface area of the N/P-doped CNF/TiO<sub>2</sub> composite by increasing its mesopore volume fraction. The mesoporous structure of the N/P-doped CNF/TiO<sub>2</sub> composite shortened its lithium ion diffusion pathways, which is beneficial for improving the performance of LIB electrodes [34].

EIS measurements were carried out using fresh cells to examine the electrochemical kinetics related to the lithium ion diffusion and charge transfer resistance of the samples. The Nyquist plots for all the electrodes

at open-circuit potentials are shown in Fig. 7(a). The semicircle in the high-frequency region corresponds to the charge transfer resistance ( $R_{ct}$ ) at the electrode/electrolyte interface. The  $R_{ct}$  values of the bare CNF, N-doped CNF/TiO<sub>2</sub>, and N/P-doped CNF/TiO<sub>2</sub> electrodes were lower than that for the TiO<sub>2</sub> NP electrode [33, 39]. This suggests that the N-doped C facilitated faster reaction kinetics between the electrode and the electrolyte and increased the electrical conductivity of the electrodes. In addition, the slanted line in the low-frequency region represents the Warburg impedance imputed to the interfacial diffusion resistance of lithium ions [33, 39]. The N/P-doped CNF/TiO<sub>2</sub> electrode showed the lowest Warburg impedance because of its shortest lithium ion diffusion pathway and highest electrical conductivity. Thus, P-doping improves the high-rate performance of CNF-based LIB electrodes. Moreover, the lithium ion diffusion coefficient could be derived from the Warburg impedance slope, according to the following equation [33, 39]:

**Table 1.** Specific surface areas, Total pore volumes, Average pore diameters, and Pore volume fractions of TiO<sub>2</sub> NPs, bare CNF, N-doped CNF/TiO<sub>2</sub>, and N/P-doped CNF/TiO<sub>2</sub>.

Samples	$S_{BET}$ [m <sup>2</sup> g <sup>-1</sup> ]	Total pore volume (p/p <sub>0</sub> =0.990) [cm <sup>3</sup> g <sup>-1</sup> ]	Average pore diameter [nm]	Pore volume fraction	
				$V_{micro}$ (%)	$V_{meso}$ (%)
TiO <sub>2</sub> NPs	52	0.37	28.4	97.3	2.7
Bare CNF	71	0.058	1.94	88.7	11.3
N-doped CNF/TiO <sub>2</sub>	97	0.051	2.103092784	84.4	15.6
N/P-doped CNF/TiO <sub>2</sub>	99	0.115	5.813888889	52.1	47.9

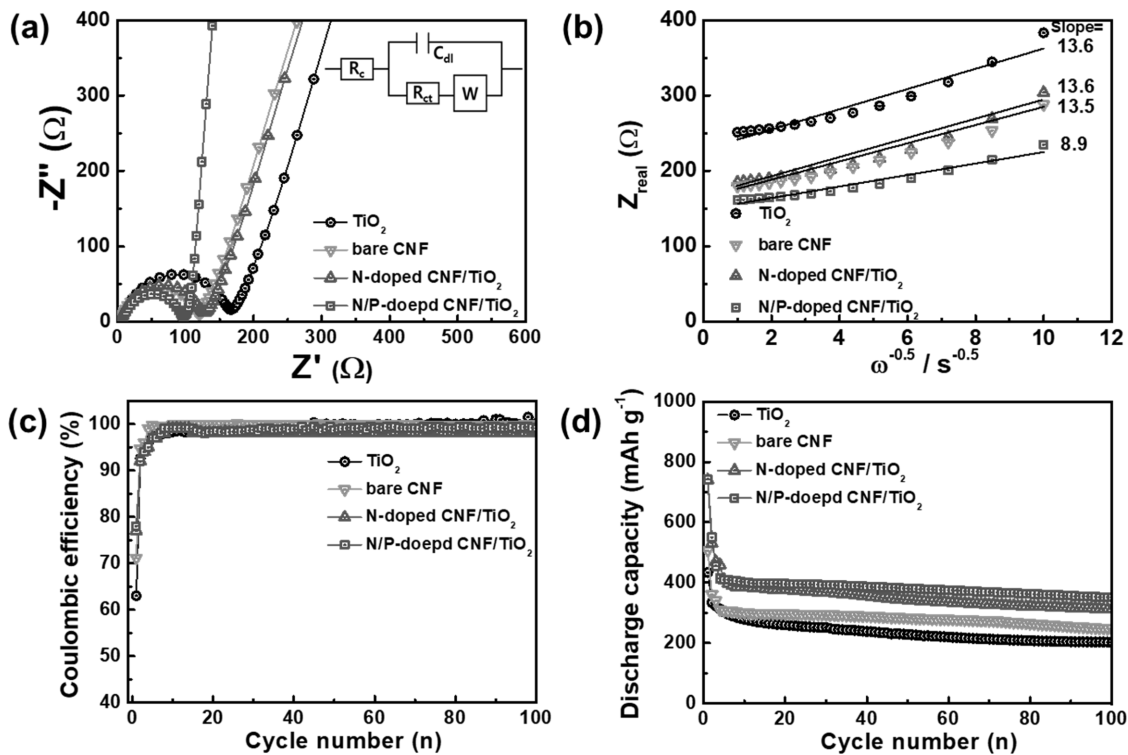


**Fig. 7.** (a) Nyquist plots in the frequency range of  $10^5$ - $10^{-2}$  Hz and (b) the relationships between  $Z_{real}$  and  $\omega^{-1/2}$  in low frequency range, (c) coulombic efficiency, and (d) cycling stabilities of TiO<sub>2</sub>, bare CNF, N-doped C/TiO<sub>2</sub>, and N/P-doped C/TiO<sub>2</sub> electrodes at 100 mA g<sup>-1</sup> during 100 cycles.

$$Z_{real} = R_e + R_{ct} + \sigma_W \omega^{-1/2} \quad (1)$$

$$D = R^2 T^2 / 2 A^2 n^4 F^4 C^2 \sigma_W^2 \quad (2)$$

where  $\sigma_W$  is the Warburg impedance coefficient,  $D$  is the lithium diffusion coefficient,  $R$  is the gas constant,  $T$  is temperature,  $A$  is the electrode area,  $n$  is the number of electrons/molecules,  $F$  is the Faraday's constant, and  $C$  is the molar concentration of lithium ions. Fig. 7(b) shows the relationship between the  $Z_{real}$  and  $\omega^{-1/2}$  of the samples in the low-frequency region. The  $\sigma_W$  values of the TiO<sub>2</sub> NP, bare CNF, N-doped CNF/TiO<sub>2</sub>, and N/P-doped CNF/TiO<sub>2</sub> electrodes were 13.6, 13.5, 13.6, and 8.9  $\Omega\text{cm}^2\text{s}^{-1/2}$ , respectively. Thus, the lithium ion diffusion coefficients of the TiO<sub>2</sub> NP, bare CNF, N-doped CNF/TiO<sub>2</sub>, and N/P-doped CNF/TiO<sub>2</sub> electrodes were calculated to be  $1.78 \times 10^{-13}$ ,  $1.81 \times 10^{-13}$ ,  $1.79 \times 10^{-13}$ , and  $4.16 \times 10^{-13}$ , respectively. These results show that the increase in the number of mesopores by P doping shortened the lithium ion diffusion pathway of the electrodes during cycling, thereby improving their lithium ion diffusion performance to facilitate ultrafast charging/discharging.

The electrochemical performances of the electrodes were evaluated by carrying out their cycling tests using coin-type cells. The Coulombic efficiencies of the electrodes were measured at the current density of 100  $\text{mA g}^{-1}$  for 100 cycles, as shown in Fig. 7(c). The electrodes showed low Coulombic efficiencies during

the first cycle because of the formation of solid-electrolyte interface (SEI) layers on their surfaces. As is well-known, SEI layers are generally formed by the reductive decomposition of the electrolyte components at the electrode surface, leading to an initial irreversible reaction. The initial Coulombic efficiencies of the TiO<sub>2</sub> NP, bare CNF, N-doped CNF/TiO<sub>2</sub>, and N/P-doped CNF/TiO<sub>2</sub> electrodes were 63%, 71%, 77%, and 78%, respectively. This indicates that the TiO<sub>2</sub> NPs dispersed in the CNF matrix contributed to the high Coulombic efficiencies of the composite electrodes during the first cycle. All the samples showed a Coulombic efficiency of nearly 100% after six cycles, indicating the occurrence of highly reversible LIB reactions.

Fig. 7(d) shows the cycling performances of all the samples at the current density of 100  $\text{mA g}^{-1}$  for 100 cycles. Fig. 7(c) shows that all the samples exhibited excellent cycling stability after 100 cycles. The discharge-specific capacities of the TiO<sub>2</sub> NP, bare CNF, N-doped CNF/TiO<sub>2</sub>, and N/P-doped CNF/TiO<sub>2</sub> samples were measured to be 202.6, 248.4, 311.9, and 351.5  $\text{mAh g}^{-1}$ , respectively. The N-doped CNF/TiO<sub>2</sub> and N/P-doped CNF/TiO<sub>2</sub> electrodes showed higher discharge-specific capacities than the other two samples because of the presence of well-dispersed TiO<sub>2</sub> NPs in their CNF matrices. These TiO<sub>2</sub> NPs provided a large number of lithium storage sites to the electrodes. In addition, the doped P atoms contributed to the high discharge-specific capacity of the N/P-doped CNF/TiO<sub>2</sub> electrode

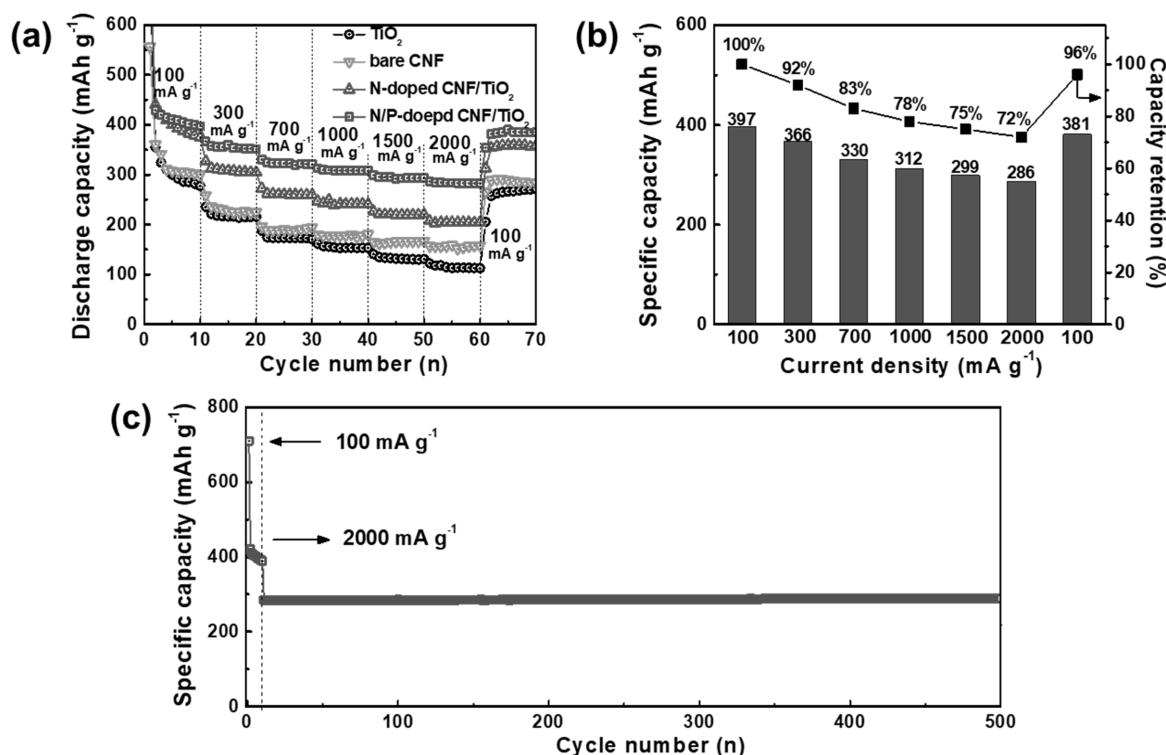


**Fig. 8.** (a) The rate performance, (b) the detailed specific capacities and capacity retentions at various current densities of 100, 300, 700, 1,000, 1,500, and 2,000  $\text{mA g}^{-1}$ , and (c) ultrafast cycling stability at current density of 2,000  $\text{mA g}^{-1}$  over 500 cycles of N/P-doped C/TiO<sub>2</sub> electrode.

by increasing its specific surface area and the number of active sites in it. With the rapid growth of the LIB industry, the need for electrodes with ultrafast charge/discharge ability and cycling stability has increased tremendously. The rate performances of the TiO<sub>2</sub> NP, bare CNF, N-doped CNF/TiO<sub>2</sub>, and N/P-doped CNF/TiO<sub>2</sub> electrodes at the current densities of 100, 300, 700, 1,000, 1,500, 2,000, and 100 mA g<sup>-1</sup> are shown in Fig. 8(a). The specific capacity of the all the electrodes decreased with an increase in the current density because of the reduction in the time available for lithium ion diffusion. The TiO<sub>2</sub> NPs showed poor high-rate performance owing to their low ion conductivity. However, N-doped C showed higher ion conductivity than TiO<sub>2</sub> NPs. Hence, the bare CNFs and N-doped CNF/TiO<sub>2</sub> showed better high-rate performance than the TiO<sub>2</sub> NPs. The N/P-doped CNF/TiO<sub>2</sub> electrode showed the best high-rate performance among all the electrodes because of the presence of P atoms in its CNF matrix. To further examine the high-rate performance of N/P-doped CNF/TiO<sub>2</sub>, its specific capacities and capacity retentions at different current densities were determined (Fig. 8(b)). The capacity of N/P-doped CNF/TiO<sub>2</sub> decreased from 397 to 381 mAh g<sup>-1</sup> with an excellent capacity retention of 96% after the current density was recovered to 100 mA g<sup>-1</sup>. This ultrafast cycling capacity of N/P doped CNF/TiO<sub>2</sub> can be attributed to its high mesopore volume caused by the doped P atoms, which provided shorter ionic diffusion lengths and accelerated the charge transfer. The N/P-doped CNF/TiO<sub>2</sub> electrode showed ultrafast cycling stability with a specific capacity of 285 mAh g<sup>-1</sup> during 500 cycles (Fig. 8(c)). As TiO<sub>2</sub> is a stable cycling material, when it is compounded with a carbon matrix as the buffer layer for volume expansion during ultrafast cycling, ultrafast cycling stability is achieved. The ultrafast cycling stability of N/P-doped CNF/TiO<sub>2</sub> can also be attributed to the improvement in its electrical properties caused by the synergistic effect of the doped N and P atoms. This resulted in the uninterrupted supply of electrons and ions along with the formation of C-N and C-P bonds under the ultrafast cycling condition.

## Conclusions

In this study, we synthesized a N/P-doped CNF/TiO<sub>2</sub> composite for application as an LIB anode using the hydrothermal, electrospinning, and carbonization techniques. TiO<sub>2</sub> NPs were well-dispersed in the N/P-doped CNF matrix. The N/P-doped CNF/TiO<sub>2</sub> electrode showed outstanding LIB performance with excellent specific capacity (351.5 mAh g<sup>-1</sup> at 100 mA g<sup>-1</sup> after 100 cycles), high rate performance (286 mAh g<sup>-1</sup> at 2000 mA g<sup>-1</sup>), and ultrafast cycling stability (285 mAh g<sup>-1</sup> at 2000 mA g<sup>-1</sup> after 500 cycles). This excellent LIB performance of the electrode can be attributed to the following: (I)

the improved specific capacity and a large number of lithium storage sites offered by the TiO<sub>2</sub> NPs, which were well-distributed in the CNF matrix; (II) the increased specific surface area caused by the increase in the number of mesopores, offering shorter lithium ion diffusion lengths; (III) the excellent electrical properties offered by the synergistic effects of the N and P dopants, leading to a continuous and uninterrupted supply of electrons and ions along with the formation of C-N and C-P bonds under the ultrafast cycling condition.

## Acknowledgement

This study was supported by the Research Program funded by the SeoulTech (Seoul National University of Science and Technology)

## References

1. M. Armand and J. -M. Tarascon, *Nature* 451 (2008) 652-657.
2. P. G. Bruce, B. Scrosati, and J.-M. Tarascon, *Angew. Chem. Int. Ed.* 47 (2008) 2930-2946.
3. Y.-T. Park and K.-T. Lee, *J. Ceram. Process. Res.* 19[3] (2018) 257-264.
4. G.-H. An, D.-Y. Lee, and H.-J. Ahn, *ACS Appl. Mater. Interfaces* 8 (2016) 19466-19474.
5. G.-H. An, D.-Y. Lee, Y.-J. Lee, and H.-J. Ahn, *ACS Appl. Mater. Interfaces* 8 (2016) 30264-30270.
6. G.-H. An, J.I. Sohn, and H.-J. Ahn, *J. Mater. Chem. A* 4 (2016) 2049-2054.
7. G.-H. An, D.-Y. Lee, and H.-J. Ahn, *ACS Appl. Mater. Interfaces* 9 (2017) 12478-12485.
8. Y.-T. Park, Y. K. Hong, and K.-T. Lee, *J. Ceram. Process. Res.* 18[7] (2017) 488-493.
9. M. Qi, Y. Zhong, M. Chen, Y. Dai, and X. Xia, *J. Alloy. Compd.* 750 (2018) 715-720.
10. Y. Teng, M. Mo, Y. Li, J. Xue, and H. Zhao, *J. Alloy. Compd.* 744 (2018) 712-720.
11. C. Zhu, C.-G. Han, G. Saito, and T. Akiyama, *J. Alloy. Compd.* 689 (2016) 931-937.
12. M. Li, X. Li, W. Li, X. Meng, Y. Yu, and X. Sun, *Electrochem. Commun.* 57 (2015) 43-47.
13. S. Brutti, V. Centili, H. Menard, B. Scrosati, and P.G. Bruce, *Adv. Energy Mater.* 2 (2012) 322-327.
14. G. Zampardi, E. Ventosa, F. L. Mantia, and W. Schumann, *Chem. Commun.* 49 (2013) 9347-9349.
15. D. Bresser, E. Paillard, E. Binetti, S. Krueger, M. Striccoli, M. Winter, and S. Passerini, *J. Power Sources* 206 (2012) 301-309.
16. Z. Yang, D. Choi, S. Kerisit, K. M. Rosso, D. Wang, J. Zhang, G. Graff, and J. Liu, *J. Power Sources* 192 (2009) 588-598.
17. M.-C. Kim, Y.-W. Lee, S.-J. Kim, B.-M. Hwang, H.-C. Park, E.-T. Hwang, G. Cao, and K.-W. Park, *Electrochim. Acta* 147 (2014) 241-249.
18. Z. Wang, J. Sha, E. Liu, C. He, C. Shi, J. Li, and N. Zhao, *J. Mater. Chem. A* 2 (2014) 8893-8901.
19. B.-S. Lee, S.-B. Son, K.-M. Park, J.-H. Seo, S.-H. Lee, I.-S. Choi, K.-H. Oh, and W.-R. Yu, *J. Power Sources* 206 (2012) 267-273.

20. Y. Chen, P. Jiang, W. Dong, and B. Huang, *Renew. Energy* 84 (2015) 130-137.
21. X. Ki, B. Zhou, W. Wang, Z. Xu, N. Li, L. Kuang, C. Li, W. Mai, H. Fu, and H. Lv, *J. Alloy. Compd.* 706 (2017) 103-109.
22. B. Xu, S. Hou, G. Cao, F. Wu, and Y. Yang, *J. Mater. Chem.* 22 (2012) 19088-19093.
23. Z. Li, Z. Xu, X. Tan, H. Wang, C. M. B. Holt, T. Stephenson, B. C. Olsen, and D. Mitlin, *Energy Environ. Sci.* 6 (2013) 871-878.
24. J.P. Paraknowitsch and A. Thomas, *Energy Environ. Sci.* 6 (2013) 2839-2855.
25. K. Wang, M. Xu, X. Wang, Z. Gu, Q. H. Fan, W. Gibbons, and J. Croat, *RSC Adv.* 7 (2017) 8236-8240.
26. Y. Zhang, W. Dai, Y. Liu, and B. Ma, *RSC Adv.* 7 (2017) 8250-8257.
27. H. Chen, F. Sun, J. Wang, W. Li, W. Qiao, L. Ling, and D. Long, *J. Phys. Chem. C* 117 (2013) 8318-8328.
28. D. Zhang, L. Zheng, Y. Ma, L. Lei, Q. Li, Y. Lim, H. Luo, H. Feng, and Y. Hao, *ACS Appl. Mater. Interfaces* 6 (2014) 2657-2665.
29. S. Some, J. Kim, K. Lee, A. Kulkarni, Y. Yoon, S. Lee, T. Kim, and H. Lee, *Adv. Mater.* 24 (2012) 5481-5486.
30. G.-H. An and H.-J. Ahn, *J. Power Sources* 272 (2014) 828-836.
31. G.-H. An, S.-J. Kim, K.W. Park, and H.-J. Ahn, *ECS Solid State Lett.* 3 (2014) M21-M23.
32. G.-H. An, E.-H. Lee and, H.-J. Ahn, *Phys. Chem. Chem. Phys.* 18 (2016) 14859-14866.
33. K. P. Singh, E. J. Bae, and J.-S. Yu, *J. Am. Chem. Soc.* 137 (2015) 3165-3168.
34. G.-H. An and H.-J. Ahn, *J. Alloy. Compd.* 710 (2017) 274-280.
35. Y. Liang, N. Li, F. Li, Z. Xu, Y. Hu, M. Jing, K. Teng, X. Yang, and J. Shi, *Electrochim. Acta* 297 (2019) 1063-1070.
36. D.-Yo. Shin, K.-W. Sung, and H.-J. Ahn, *Appl. Surf. Sci.* 478 (2019) 499-504.
37. G.-H. An, T.-K. Lee, and H.-J. Ahn, *J. Korean Powder Metall. Inst.* 22 (2015) 367-375.
38. G.-H. An, B.-R. Koo, and H.-J. Ahn, *Phys. Chem. Chem. Phys.* 18 (2016) 6587-6594.
39. G.-H. An and H.-J. Ahn, *Carbon* 65 (2013) 87-96.